Faraday Discussions

Petahertz charge dynamics in a correlated organic superconductor

Journal:	*Faraday Discussions*
Manuscript ID	FD-ART-01-2022-000004
Article Type:	Paper
Date Submitted by the Author:	10-Jan-2022
Complete List of Authors:	Iwai, Shinichiro; Tohoku University Graduate School of Science and Faculty of Science Kawakami, Yohei; Tohoku University Graduate School of Science and Faculty of Science Itoh, Hirotake; Tohoku University Graduate School of Science and Faculty of Science Yonemitsu, Kenji; Chuo University Faculty of Science and Engineering Graduate School of Science and Engineering

ARTICLE

Petahertz charge dynamics in a correlated organic superconductor

Shinichiro Iwai*[a], Yohei Kawakami[a], HIrotake Itoh[a], and Kenji Yonemitsu[b]

Received 00th January 20xx,
Accepted 00th January 20xx

DOI: 10.1039/x0xx00000x

We report an observation of stimulated emission induced by a nearly single-cycle 6 fs near infrared electric field of 10 MV/cm in an organic superconductor (κ-(h-ET)$_2$Cu[N(CN)$_2$]Br). The stimulated emission is attributed to a non-linear synchronized coherent charge oscillation. We also report that, in the same organic superconductor, a light-induced current before the scattering time shows up as carrier-envelope phase (CEP)- sensitive second harmonic generation (SHG). This unconventional SHG in the cetrosymmetric compound is regarded as a light induced spatial symmetry breaking. These ultrafast optical non-linearities induced by petahertz charge oscillations show anomalous enhancements around the superconducting transition temperature (11.6 K). These results indicate that the microscopic mechanism of superconducting fluctuations is closely related to the Coulomb repulsive interaction in this compound.

Introduction

A Ultrafast charge dynamics in organic superconductor within no-scattering time window

Superconductors are characterized by a gap (superconducting energy gap) for the excitation of quasi-particles with an energy of ca. meV. However, the electronic properties of the superconductivity are not necessary determined only by such low-energy interactions [1-3]. It is well known that competing energetic factors such as Coulomb repulsion (U) and inter-site hopping (t) as well as contributions from a spin-orbit interaction and/or an antiferromagnetic interaction play important roles in strongly correlated electron systems as shown in Fig. 1. Such hierarchy on the energy (time) axis is useful for understanding the electronic and magnetic properties of superconductors with strong electron correlations such as high-temperature superconducting cuprates and organic superconductors.

However, it is not necessarily true that there is no relation between Coulomb repulsion (>1 eV) and the superconducting gap (~meV), although the former is 3-orders of magnitude larger than the latter. In fact, contributions of anti-ferromagnetic interactions and Coulomb repulsion are suggested to be important for the high superconducting transition temperature (High-T_{SC}), the isotope effects and the symmetry of the d-wave pairing. If we assume that the microscopic origin of the superconductivity is related to the Coulomb repulsion (on the order of 1 eV (organic conductors) and 10 eV (cuprates)), ultrafast responses on the time scales of several hundreds of attosecond (as) or several femtoseconds are expected to be realized. Photoexcitation of

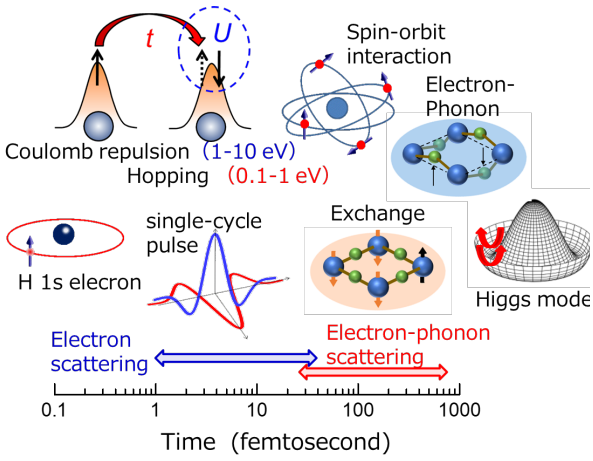

Fig. 1 (a) Time scales of various interactions in strongly

superconductors by visible or near infrared lights is known as a mechanism for superconducting photodetection. This optical response has been understood as the generation of quasi-particles [4] which necessary results in an increase in the electron temperature or equivalently a disappearance of electronic coherence, losing the controllability of the non-equilibrium state. A low-energy excitation by THz or mid -IR lights is an excellent solution for the problem [5-8]. But, here, we focus on another approach. It is to complete the excitation before the increase in the electron temperature (or before the electron scattering processes become dominant).

In some materials, including organic compounds, the increase in the electron temperature needs ca. 40 fs (corresponding to the energy scale of 0.1 eV= $\hbar$/40 fs) [9]. If we use a several-femtosecond pulse for those compounds, we can control charge motion before the increase in the electron temperature. In such

[a] Department of Physics, Tohoku University, Sendai 980-8578, Japan
[b] Department of Physics, Chuo University, Tokyo 112-8551, Japan

a no-scattering time window, any degree of freedom hardly reaches equilibrium, and the electronic coherence survives on the time scale from several to several tens of femtoseconds which correspond to the energy scale of the inter-site hopping.

This is a new pathway toward the ultrafast control of correlated electrons. In fact, we have realized the coherent modulation of the electronic state before the scattering time by using a 7- or 6-fs, nearly single-cycle pulse in an organic metal [10-14]. Thus, the excitation within the ultrafast time window is the key issue for realizing coherent charge dynamics which is not disturbed by scattering processes.

Here, we focus on the petahertz charge dynamics in an organic superconductor (κ-(h-ET)$_2$Cu[N(CN)$_2$]Br) [13]. We report an observation of stimulated emission induced by a nearly single-cycle 6 fs near infrared electric field. The stimulated emission is attributed to a non-linear synchronized coherent charge oscillation. We also report that, in the same organic superconductor, a light-induced current before the scattering time driven by the 6 fs pulse shows up as second harmonic generation (SHG), which is regarded as a light-induced spatial symmetry breaking in this centrosymmetric compound [14].

B Organic superconductor κ-(h-ET)$_2$Cu[N(CN)$_2$]Br (h-Br)

κ-(h-ET)$_2$Cu[N(CN)$_2$]Br (h-Br) (ET; bis[ethylenedithio]-tetrathiafulvalene) shown in Fig. 2(a) is a well-known layered organic superconductor with a superconducting transition temperature of T_{SC}=11.6 K [15-21]. The triangular lattice consisting of ET dimers is effectively regarded as a 1/2-filled system, although the averaged charge per ET molecule is +0.5 (3/4 filling). The temperature-bandwidth phase diagram of κ-(ET)$_2$X (X; anion molecule), where the bandwidth is proportional to the inter-site hopping, is characterized by the first-order Mott transition line and the critical end point (T_{END}=33 K) as shown in Fig. 2(b). Superconducting fluctuations toward T_{SC} below 2T_{SC} have been discussed in terms of a short-range correlation of the Cooper pairs [22, 23].

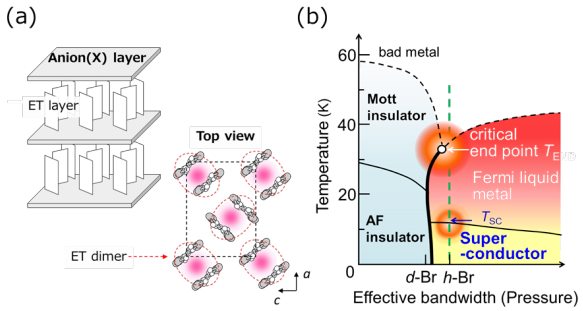

Fig. 2 **(a)** Schematic illustrations of crystal structure and triangular lattice of ET dimers in κ-(ET)$_2$X. **(b)** Temperature-bandwidth phase diagram.

Experimental

a Sample preparations

Single crystals of h-Br (typically 0.7 × 0.5 × 0.8 mm for a, b, and c-axes, respectively) and a thin film of h-Br (0.5 × 1.8×10^{-4} ×0.5 mm on a CaF_2 substrate with the thickness of 0.5 mm) were prepared using the methods described in previous studies [20, 24].

b 6 fs infrared pulse generation and pump-probe measurements

A broadband infrared spectrum covering 1.2–2.3 μm of the 6 fs pulse is obtained by focusing a carrier-envelope phase (CEP) stabilized idler pulse (1.7 μm) from an optical parametric amplifier (Quantronix HE-TOPAS pumped by Spectra-Physics Spitfire-Ace) onto a hollow fibre set within a Kr-filled chamber (Femtolasers). Pulse compression is performed using both active mirror (OKO, 19-ch linear MMDM) and chirped mirror (Femtolasers and Sigma-Koki) techniques [10-14].

We performed transient reflectivity and absorption measurements for the single crystal and the thin film [24] using the 6 fs pulse. In these measurements, the intensity of the pump pulse is controlled in the wide range from 0.01 to 2 mJ/cm^2 with a step of 0.006 mJ/cm^2 by a pair of wire-grid CaF_2 polarizers [12]. In the transient reflectivity/absorption measurement, the probe pulse reflected/transmitted from the sample is detected by InGaAs detectors (New-Focus model 2034) after passing through spectrometers (JASCO, M10). We also perform a

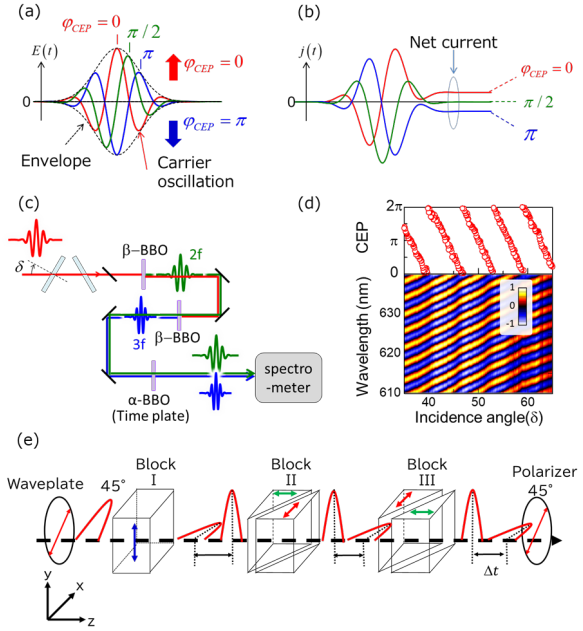

Fig. 3 **(a)(b)** Schematic illustrations of single-cycle light field *E*(t) and current j(t) induced by no-scattering charge acceleration (see main text), respectively. **(c)** Set-up of 2f-3f interferometer to detect a relative change in the CEP which is controlled by a pair of glass plates (δ: incidence angle). **(d)** Lower panel; Interference spectra between 2f and 3f as a function of δ. Upper panel: Relative CEP (obtained from 2f-3f spectra) as a function of δ. **(e)** Schematic illustration of TWINS [28, 29] using α-BBO (negative uniaxial crystal). The blue, red and green arrows indicate the optical axes (fast axis) for the birefringent plate (Block I) and wedges (in Blocks II and III).

transient reflectivity measurement with a double-pump pulse which is generated by the Michelson interferometer.

c Measurement and CEP dependence of SHG

We performed SHG and third harmonic generation (THG) measurements for the single crystal using a 6 fs pulse with a reflection geometry (incident angle is smaller than 3-degree). The fundamental photon energy is 0.75 eV. The intensity and polarization of the fundamental pulse (excitation range: 0.01 to 2 mJ/cm^2) are controlled by a pair of wire-grid CaF_2 polarizers [12]. The SHG and the THG are detected by a photomultiplier tube (Hamamatsu R13456) after passing through a spectrometer (JASCO, M10).

The CEP of the fundamental pulse (Fig. 3(a)) is controlled by a pair of glass plates [25, 26] (BK-7 with a thickness of 1 mm) with the incident angle of δ (Fig. 3(c)) and detected by the 2f-3f interferometer [27] (2f and 3f are generated using β-BBO) [Figs. 3(c) and 3(d)].

d Measurement of 4th order nonlinear polarization

In the measurement of higher (>4-th) order harmonic generations (HHGs), absorption losses sometimes prevent the detection because of various optical transitions such as intramolecular transitions above the low-energy charge gap in strongly correlated materials. In fact, h-Br has a large absorption loss above 3 eV, although there is a spectral window between 0.6-2.5 eV for SHG and THG. Here, we observe 4-th order polarization by measuring SHG and THG that can be modulated by higher order polarizations. It is understood from the concept of 2-D spectroscopy [28-31], i.e., one axis of the 2 dimensions (2-D) is set up by the conventional dispersion spectrometer, and the other is obtained by the Fourier transform of the interferogram (see also Figs. 11(a) and 11(b)).

A pair of pulses with a time difference of Δt enters the material and emitted SHG and THG are detected by changing Δt. Here, Δt is scanned with an accuracy of < 100 attoseconds by using the TWINS (Translating -Wedge-Based Identical Pulses eNcoding System) technique (Fig. 3(e) [28, 29] for a 1-2 micron range. The TWINS consists of birefringent plates and wedges of α-BBO (a negative uniaxial birefringent material). In Fig.3 (e), the y polarization component of incident 45-degree (in the x-y plane) polarization light advances in comparison with the x polarization component after Block I with the fast axis of y (blue arrow). Then, the y polarization component is delayed by propagating in the wedge with the fast axis of x (red arrow) in Block II. By moving Block II along the x axis, we can change the time difference between the x- and the y- polarized pulses with an accuracy of < 100 attoseconds. Block III is used to compensate the changes of dispersions. Finally, the 45° components from both the pulses are extracted to obtain the double-pulse in the same polarization. The interferogram (light intensity as a function of Δt) is detected at the wavelengths of SHG and third harmonic generation (THG). A modulation induced by the 4-th order polarization is obtained in the Fourier transformed spectra of the interferograms. That is a part of non-linear 2-D spectroscopy where the interplay between different order harmonics is detected as an off-diagonal component (see Fig. 11(b)).

Results and discussion

A Stimulated emission induced by synchronized charge motion

Figure 4(a) shows steady-state reflectivity (R) and transient reflectivity (ΔR/R) spectra of a single crystal of h-Br. The polarization of the pump and probe pulses are parallel to the **c**-axis. The excitation intensity (I_{ex}) and the time delay between the pump and probe pulses (t_d) are 1.0 mJ/cm^2 (corresponding to 11 MV/cm) and 10 fs (red line), 200 fs (magenta line), and 500 fs (violet line), respectively. A large increase in R (ΔR/R~180% at 0.63 eV) is observed at 10 fs on the higher energy side of the dimer band which has been assigned to the transition from the bonding to antibonding states of an ET dimer in Fig. 2(a). The spectral width of the peak at t_d = 200 fs (0.04 eV=$\hbar$/(100 fs)), which is much narrower than that of the dimer band (170 meV), is roughly consistent with the time constant of the fast decay component (70 fs as described later).

At shorter t_d=10 fs, the ΔR/R spectrum has a broad tail with structures reflecting the uncertainty relation between time and frequency. That is a so-called coherent artifact and does not include information of the material. The transient reflectivity and transient transmittance (ΔT/T) of a 180 nm thin film on the same experimental conditions are shown in Fig. 4(b). We notice that ΔT/T shows a large increase (~20%) at 0.67 eV. We confirmed that ΔT/T in the CaF_2 substrate is negligible. Note that ΔR/R>0 and ΔT/T>0 in the same

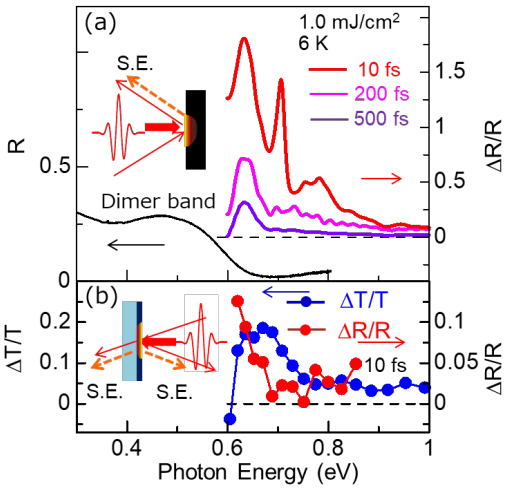

Fig. 4 **(a)** Transient reflectivity (ΔR/R) and steady-state reflectivity (R)spectra (||**c**) of a single crystal for I_{ex} = 1.0 mJ/cm^2 at time delays of 10 fs, 200 fs, and 500 fs. **(b)** Transient reflectivity (ΔR/R) and transmittance (ΔT/T) spectra of 180 nm thin film κ-(BEDT-TTF)$_2$Cu[N(CN)$_2$]Br for I_{ex} = 1.0 mJ/cm^2 at 10 fs. S.E in the inset shows stimulated emission.

spectral range in Fig. 4(b) are ascribed to stimulated emission or equivalently an optical gain.

Figure 5(a) shows the time profile of ΔR/R peak at I_{ex}=1.0 mJ/cm², which is reproduced by using the conventional method as shown by the black line obeying the equation,

$$\Delta R(t)/R = \int_{-\infty}^{+\infty} K(t)G(t-t')dt'$$

$$K(t) = A_{fast}[1-\exp(-t/\tau_{frise})]\exp\left(-\frac{t}{\tau_f}\right) + [1-\exp(-t/\tau_{s-rise})]\sum_{n=1}^{3} A_{slow\,n}\exp\left(-\frac{t}{\tau_{sn}}\right)$$

$$G(t) = \exp[-4ln2\,t^2/\{(9\,(fs))^2\}]$$

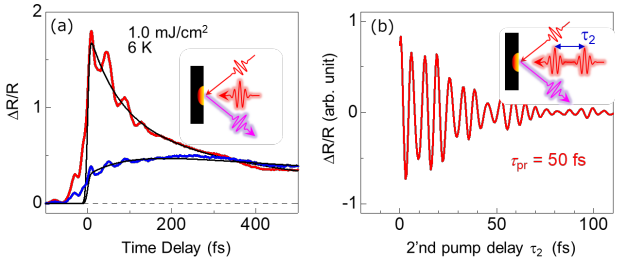

Fig. 5 **(a)**Time profiles of ΔR/R peak (0.63 eV) at I_{ex}=1.0 mJ/cm² (red line) and I_{ex}=0.1 mJ/cm²(blue line) which are analyzed by using the conventional method (black curves; see main text). **(b)** Oscillating component of ΔR/R at 0.63 eV as a function of time difference between two pump pulses (τ_2) in transient reflectivity measurement with double-pump pulse (6K, 1mJ/cm²). The delay between the second pump and the probe pulses is set at τ_{pr}=50 fs.

, where the gaussian G(t) with a width of time resolution (=9 fs) is an instrumental response function. A_{fast} and $A_{slow\,n}$ (n = 1~3) represent the coefficients for the fast and slow components. For the red line in Fig. 5(a) (I_{ex} = 1.0 mJ cm^{-2}), the fast build-up ($\tau_{f\text{-}rise}$ < 5 fs) with decay (τ_f = 70 fs) is dominant (65.4%) in comparison with the slow rise ($\tau_{s\text{-}rise}$=90 fs) with three-component decay τ_{s1} = 360 fs (29.7%), τ_{s2} = 4.2 ps (1.3%), τ_{s3} > 100 ps (3.6%) and the oscillation (period 43 fs, damping time 70 fs, initial phase, -0.15π). For the blue line in Fig. 5(a) [I_{ex} = 0.1 mJ cm^{-2} (×4)], the fast component (with same $\tau_{f\text{-}rise}$ and τ_f) is smaller (32.2%), while the slow rise is dominant (67.8%; τ_{s1} = 360 fs (20.8%), τ_{s2} = 2.2 ps (45.5%), τ_{s3} > 100 ps (1.5%)). The oscillating component with a period of 43 fs in the time profile is attributed to a coherent intra-molecular vibration [$\nu_{60}(B_{3g})$] which strongly interacts with the electronic state [32, 33]. Thus, the fast rise ($\tau_{f\text{-}rise}$ < 5 fs)-and-decay (τ_f =70 fs) component of ΔR/R reflecting the stimulated emission becomes dominant for the strong excitation.

Recall that the spectral width of the peak (0.04 eV =ħ/(100 fs)) at t_d=200 fs, which is much narrower than that of the dimer band (0.17 eV) shown in Fig. 4(a), is roughly consistent with the time constant of the fast decay component of 70 fs. This fact suggests that the stimulated emission is induced by only one electronic mode which is selectively driven in a coherent manner avoiding dissipation. To confirm such electronic coherence, we perform transient reflectivity measurement with two pump pulses. Such double-pulse experiments have been used for investigating electronic coherence of the photoinduced phase [34] or coherent phonons [35]. In our case, we can measure the coherence at the origin of the stimulated emission.

Figure 5(b) shows an oscillating component of ΔR(t)/R measured at 0.63 eV as a function of the time difference between the two (the first and the second) pump pulses (τ_2) (6K, 1 mJ/cm² for the respective pump pulses). The delay between the second pump and the probe pulses is set at 50 fs (within the lifetime of the stimulated emission). The observed oscillation shows a dephasing time of ca. 40 fs, indicating that the coherence induced by the pump light survives until the time much longer than the pulse duration. It is noteworthy that the coherence time obtained in this measurement is comparable to the above mentioned τ_f (70 fs) reflecting the lifetime of the stimulated emission. This fact indicates that the fast rise-and-decay component is governed by the electronic coherence. Considering that the fast component is dominant for the strong excitation, the origin of the stimulated emission is attributed to the coherent charge motion driven by the strong light field. This is very different from the conventional mechanism for the stimulated emission which is due to population inversion.

To clarify the origin of the non-linear charge motion, i.e., the ΔR/R peak at 0.63 eV (or equivalently the stimulated emission), we theoretically investigated charge oscillations which are driven by the single-cycle light-field in a two-dimensional (2D) 3/4-filled extended Hubbard model for the 16-site system [13, 36]. Fourier transform (FT) spectra of the charge-density time profile of a molecule are shown by the lower panel of Fig. 6(a). The weight of the FT spectrum for the field amplitude F=0.01 [V/A] along the **c**-axis, on-site Coulomb repulsion U=0.8 eV, nearest-neighbor Coulomb repulsions between sites i and j V_{ij}=0 [green dots in the lower panel of Fig. 6(a)] is mainly

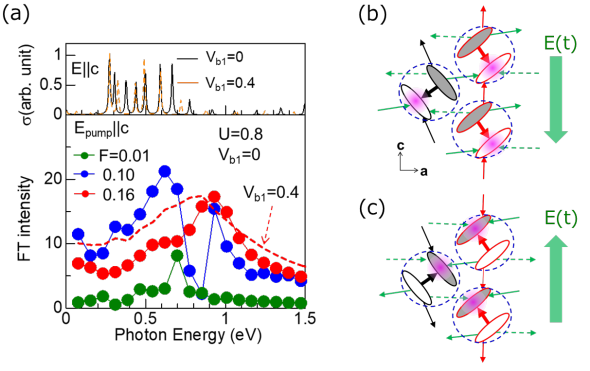

Fig. 6 **(a)** Upper panel: Calculated optical conductivity spectrum (polarization along c-axis). Lower panel: Calculated FT spectra of the charge-density time profile of a molecule for F=0.01 (green dots), 0.10(blue dots), and 0.16(red dots). **(b)(c)** Schematic illustration of charge motion through bonds, which are indicated by arrows.

distributed in ≤ 0.7 eV which is the main energy range of the steady-state optical conductivity (σ) for polarization along the **c**-axis [upper panel of Fig. 6(a)].The energy scale is slightly larger than the experimental one owing to the smallness of the system treated here. This FT spectrum for F=0.01 corresponds to linear charge-density oscillations including transitions from the bonding to anti-bonding states around a dimer. With increasing F, the spectral weight at the higher energy (~0.9 eV) region becomes dominant. This FT spectral weight is attributable to the synchronized charge oscillation [37-39] shown in Figs. 6(b) and 6(c). Also for finite V_{ij}(orange dashed line in lower panel of Fig. 6(a) for F=0.16), the spectral nature is essentially the same. This oscillation is driven by charge transfers through all the bonds between charge-rich and poor sites, i.e., charges flow into a site denoted by a white ellipse from four neighboring gray sites through the b_1, b_2, and two q bonds (Fig. 6(b)), and then charges flow back to the gray sites (Fig. 6(c)). The observed peak energy of 0.63 eV indicates that the oscillation period is ~6 fs.

The highlight of this section is an enhancement of ΔR/R near T_{SC} and T_{END}. The temperature dependence of the ΔR/R spectrum is shown for t_d=10 fs at I_{ex} =1.0 mJ/cm^2 (Fig. 7(a) upper panel) and 0.01 mJ/cm^2 (Fig. 7(a) lower panel). The 0.63 eV peak grows with lowering temperature below 50 K for both I_{ex}. The ultrafast response of ΔR/R(0.63 eV) for t_d=10 fs at large I_{ex} (Fig. 7(a) upper panel) indicates an anomalous enhancement near T_{END} (~30 K) and further increase at lower temperatures between ~2 T_{SC} and T_{SC}. It is well known that superconducting fluctuations exist in this temperature range, reflecting the short-range correlation of Cooper pairs.

The application of an I_{ex} =1.0 mJ/cm^2 (11 MV/cm) light-field is expected to increase the electron and lattice temperatures. Considering the linear coefficient of the temperature-dependent specific heat γ=22 mJ K^{-2} mol^{-1} [40], the electron temperature is finally expected to be 520 K. However, the rise in the electron temperature is negligible at t_d=10 fs (when the anomalies are observed in the temperature dependence (Fig. 7(a))) because electrons are scattered only a few times before in this compound. Note that the anomalies at ~10 K and ~28 K show 2~4 K shifts (at 1.0 mJ/cm^2) to the low-temperature side because of a heat accumulation

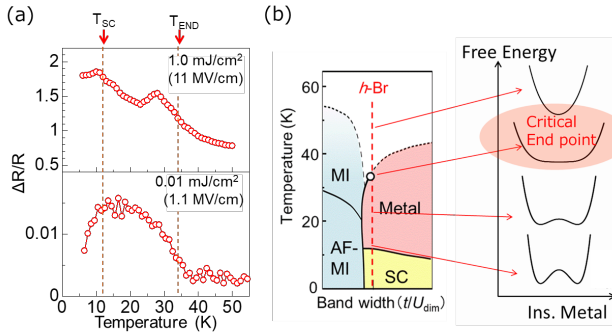

Fig. 7 **(a)**Temperature dependence of ΔR/R at 0.62 eV for t_d=10 fs (upper panel) and for I_{ex} =1.0 mJ/cm^2 (lower panel) **(b)** Temperature-bandwidth phase diagram and schematic free energy curves at the respective places in the phase diagram.

in a 1 kHz operation [13].

This ~10 fs response is in contrast to the energy scale of the superconducting gap and its fluctuation (~meV from T_{SC}=11.6 K) corresponding to a picosecond timescale. For smaller I_{ex}, on the other hand, the increase in ΔR/R below ~2T_{SC} at t_d=10 fs becomes obscure (0.01 mJ/cm^2, lower panel in Fig. 7(a)), while the anomaly at ~T_{END} remains. No anomalies are observed in the temperature dependence of ΔR/R in insulating κ-(*d*-BEDT-TTF)$_2$Cu[N(CN)$_2$]Br, which does not have T_{SC} or T_{END} located on the small t/U_{dimer} side of the phase diagram [13].

The enhancement of the non-linear charge motion at ~T_{END} can be attributed to the absence of the potential barrier for the first order phase transition (Fig. 7(b)). In such a situation, a strong light field can induce the non-linear charge response shown in Figs. 6(b) and 6(c) with a large amplitude. Since the Coulomb repulsion is larger than 0.4 eV (=$\hbar$/(10 fs), the ultrafast ~10 fs response of the anomaly at ~T_{END} is reasonable, i.e., it confirms that the insulator to metal transition is of electronic origin because the timescale of inter-molecular motion (> 200 fs) is much longer.

B Unconventional SHG induced by no-scattering current.

In this section, we focus on SHG of h-Br. This compound is centrosymmetric [16, 17] so that SHG is generally believed to be forbidden. However, it becomes active for the strong light field because of a light-induced no-scattering current.

Figure 8(a) shows spectra of SHG (red ($\boldsymbol{E}_{fund}$||**c**, $\boldsymbol{E}_{SH}$||**c**), green ($\mathbf{E}_{fund}$||**a**, $\mathbf{E}_{SH}$||**c**, x 0.73)) and THG (blue line ($\boldsymbol{E}_{fund}$||**c**, $\boldsymbol{E}_{TH}$||**c**, x0.024)) at 6 K. The respective peak energies are 1.5 eV (SHG) and 2.2 eV (THG). $\boldsymbol{E}_{fund}$, $\boldsymbol{E}_{SH}$, and $\boldsymbol{E}_{TH}$ indicate the electric fields of excitation light, second harmonic and third harmonic lights, respectively. An intensity of the SHG is ca. 1/50 times smaller than that of the THG. Note that the SHG is not active for weak fields in this compound because this compound has inversion centers (orthorhombic structure with class P_{nma}) as mentioned above. This SHG is not attributed to a surface effect because of its unconventional dependences on the temperature and the CEP as shown below.

As shown in Fig. 8(b), the temperature dependences of the SHG (for both $\boldsymbol{E}_{fund}$||**c** (closed red circles) and $\boldsymbol{E}_{fund}$||**a** (open red circles)) show clear increase toward T_{SC}, although we have no significant temperature dependence for the THG. As mentioned above, superconducting fluctuations exist in the temperature range above T_{SC}, reflecting short-range correlations of Cooper pairs. The result in

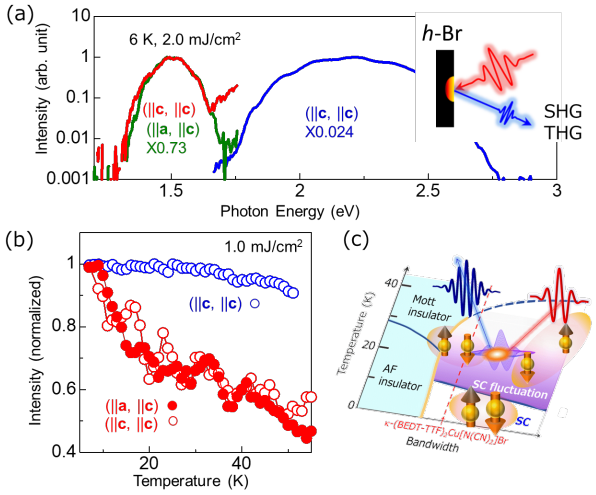

Fig. 8 **(a)** SHG spectra of h-Br (single crystal) at 6 K ($\boldsymbol{E}_{\text{fund}}||\mathbf{c}$, $\boldsymbol{E}_{\text{SH}}||\mathbf{c}$) (red line) and ($\boldsymbol{E}_{\text{fund}}||\mathbf{a}$, $\boldsymbol{E}_{\text{SH}}||\mathbf{c}$) (green line, x 0.73)). THG spectrum (x 0.024) ($\boldsymbol{E}_{\text{fund}}||\mathbf{c}$, $\boldsymbol{E}_{\text{TH}}||\mathbf{c}$) (blue line). **(b)** Temperature dependences of I_{SH} (closed red circles: $\boldsymbol{E}_{\text{fund}}||\mathbf{a}$, $\boldsymbol{E}_{\text{SH}}||\mathbf{c}$, open red circles: $\boldsymbol{E}_{\text{fund}}||\mathbf{c}$, $\boldsymbol{E}_{\text{SH}}||\mathbf{c}$) and I_{TH} (blue circles, $\boldsymbol{E}_{\text{fund}}||\mathbf{c}$, $\boldsymbol{E}_{\text{TH}}||\mathbf{c}$). Both are normalized by the respective intensities at 6 K. **(c)** Temperature-bandwidth phase diagram of κ-$(ET)_2X$, which is extracted on the basis of the controlled effective bandwidth.

Fig. 8(b) clearly indicates that the unconventional SHG is enhanced by the superconducting fluctuations as schematically shown in Fig. 8(c). Considering that the light field is applied for several femtoseconds, no-scattering charge acceleration induces a current and resultant SHG [14] as shown below.

According to common sense or if Ohm's law ($\boldsymbol{j}(\mathbf{t}) = \sigma \boldsymbol{E}(\boldsymbol{t}), \mathbf{j}: \mathbf{current}, \sigma: \mathbf{conductivity}, \boldsymbol{E}: \mathbf{electric\ field}$) holds, an oscillating light field does not give a net current because the time average of the electric field vanishes. However, the light field is applied only for 6 fs. In this case, charge acceleration is realized, resulting in a finite net current before the increase in the electron temperature. If such a finite current is generated during the no-scattering time window of ca. 40 fs in this compound, we can detect it as current induced SHG. Note that the current-induced SHGs have been observed in graphene [41, 42] and BCS superconductors [43] under DC and terahertz fields.

To demonstrate that the SHG is attributable to the no-scattering current, we measure the CEP dependence of the SHG. The time profile of the no-scattering charge current is given by the time integral of the electric field $\boldsymbol{j}(\boldsymbol{t}) \propto \int_0^t \boldsymbol{E}(\tau)\boldsymbol{d}\tau$. Figure 3(b) shows that we have a finite net current depending on the CEP before dephasing processes take place. In this case, the current density should show a one-cycle change when the CEP has a one-period change.

Figure 9(a) shows the change of the SHG intensity ($\Delta I_{\text{SH}}/I_{\text{SH}}$, I_{SH}: averaged SHG intensity for varying CEP, ΔI_{SH} is the difference

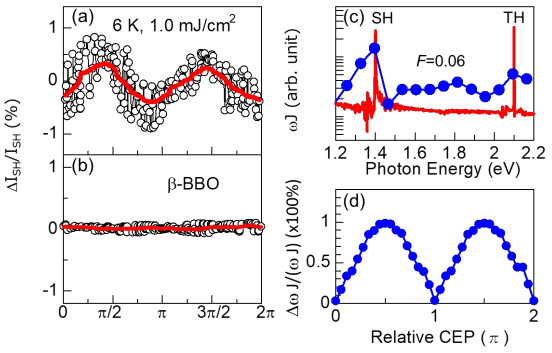

Fig. 9 **(a)** Intensity change of the SHG ($\Delta I_{\text{SH}}/I_{\text{SH}}$) as a function of relative CEP. **(b)** Reference of the conventional SHG in β-BBO (room temperature). In both (a) and (b), the red curve is obtained by averaging the data (guide to the eye). **(c)** Calculated spectra of ωJ showing SHG and THG for light-field (which is polarized parallel to the **c**-axis) F= 0.06 (red line; Hartree-Fock approximation, blue dots; exact diagonalization) **(d)** CEP dependence of the calculated SHG intensity [peak intensities of ωJ at 1.4 eV (SHG)] for F=0.1.

between the observed SHG and I_{SH}) as a function of the relative change of CEP from 0 to 2π. Figure 9(b) shows a reference of the conventional SHG in β-BBO (room temperature). We cannot detect any CEP dependence in the reference. In h-Br, we have a two-cycle change in SHG under the one-period change of the CEP. Because SHG cannot distinguish no-scattering currents with opposite directions, the two-cycle change under the one-period change of the CEP is reasonable. Thus, the observed SHG is due to a no-scattering current.

It is noteworthy that the spectral bandwidth (135 meV) is significantly narrower than that of the pump spectrum (ca. 500 meV). This fact indicates that the no-scattering current survives about 30 fs after the application of the light field. This time scale is comparable with that of the scattering time.

To clarify the origin of the SHG more in detail, we theoretically calculate the current density $\boldsymbol{j}$ in a two-dimensional three-quarter-filled Hubbard model for a 98x98-site system in the framework of the time-dependent Hartree-Fock approximation. We use the Hubbard model at three-quarter filling, $\boldsymbol{H} = \sum_{\langle i,j\rangle\sigma} \boldsymbol{t}_{ij}\left(\boldsymbol{c}_{i\sigma}^{\dagger}\boldsymbol{c}_{j\sigma} + \boldsymbol{c}_{j\sigma}^{\dagger}\boldsymbol{c}_{i\sigma}\right) + \boldsymbol{U}\sum_{i} \boldsymbol{n}_{i\uparrow}\boldsymbol{n}_{i\downarrow}$, where $\boldsymbol{c}_{i\sigma}^{\dagger}$ creates an electron in the highest occupied molecular orbital (HOMO) with spin $\boldsymbol{\sigma}$ at site $\boldsymbol{i}$, and $\boldsymbol{n}_{i\sigma} = \boldsymbol{c}_{i\sigma}^{\dagger}\boldsymbol{c}_{i\sigma}$. For the on-site Coulomb repulsion, we use $\boldsymbol{U}$ =0.8 eV. The transfer integral $\boldsymbol{t}_{ij}$ depends on the bond $\boldsymbol{ij}$. The molecular arrangement is taken from the structural data, from which $\boldsymbol{t}_{ij}$ are estimated with the extended Hückel method [16, 17]. The initial state is the Hartree-Fock ground state. Photoexcitation is introduced through the substitution $\boldsymbol{c}_{i\sigma}^{\dagger}\boldsymbol{c}_{j\sigma} \rightarrow \exp\left[\boldsymbol{ie}/\hbar\boldsymbol{c}\ \boldsymbol{r}_{ij}\cdot\boldsymbol{A}(\boldsymbol{t})\right]\boldsymbol{c}_{i\sigma}^{\dagger}\boldsymbol{c}_{j\sigma}$ with relative intermolecular position $\boldsymbol{r}_{ij} = \boldsymbol{r}_j - \boldsymbol{r}_i$. The vector potential we use is $\boldsymbol{A}(t)$=θ(t) $\boldsymbol{F}/\omega_{\text{fund}}$ [cos (ω_{fund} t-φ)-cos φ] and corresponds to $\boldsymbol{E}(t)$=θ(t) $\boldsymbol{F}$sin(ω_{fund} t-φ),with $\boldsymbol{F}$=(0, F) ||$\boldsymbol{c}$ and fundamental photon energy ω_{fund}=0.7 eV. The time-dependent Schrödinger equation is

numerically solved. We calculate the Fourier transform of the current density $\boldsymbol{j}(t)$=–⟨ ∂ H/N ∂ A⟩ with N being the number of unit cells for 500 cycles. The absolute value of its Fourier transform is denoted by J. The SHG and THG are evaluated as ωJ (the absolute value of the Fourier transform of d$\boldsymbol{j}$/dt) at $\omega=2\omega_{fund}$ and $\omega=3\omega_{fund}$ [44, 45], respectively, and shown for $\boldsymbol{E}_{SH}$||**c** and $\boldsymbol{E}_{TH}$ ||**c** with electric field amplitudes (F [V/angstrom]) of 0.06 by the red line in Fig. 9(c). The obtained bandwidth is basically determined by the time window of the Fourier transform in the Hartree-Fock simulation without dephasing. Therefore, we cannot discuss the bandwidth. I_{SH} is sensitive to the CEP (Fig. 9(d)), which is consistent with the result shown in Fig. 9(a). To check the emergence of SHG, we also calculate ωJ by using the exact diagonalization method for a 16-site system

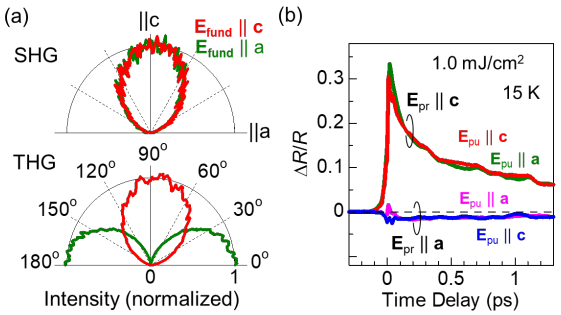

Fig. 10 (a) Polarization dependences of SHG intensities (upper panel) and THG intensities (lower panel) for $\boldsymbol{E}_{fund}$ ||**c** (red line) and $\boldsymbol{E}_{fund}$ ||**a** (green line), respectively. (b) Time evolutions of transient reflectivity change ($\Delta R/R$) measured at 0.62 eV (excitation by 6 fs, 1 mJ/cm^2 , 0.6-0.9 eV pulse, 6 K). The time profiles of $\Delta R/R$ for $\boldsymbol{E}_{pr}$||**c** are shown by the red ($\boldsymbol{E}_{pu}$||**c**) and green ($\boldsymbol{E}_{pu}$||**a**) curves. Those for $\boldsymbol{E}_{pr}$||**a** are shown by the blue ($\boldsymbol{E}_{pu}$||**c**) and magenta ($\boldsymbol{E}_{pu}$||**a**) curves.

[13, 36] during 10-cycle irradiation. The Fourier spectrum indicated by the blue dots in Fig. 9(c) clearly shows the SHG peak.

As shown in the upper panel of Fig. 10(a), the SHG is polarized parallel to the **c**-axis ($\boldsymbol{E}_{SH}$||**c**) for both excitation polarizations ($\boldsymbol{E}_{Fund}$||**c** (red line), $\boldsymbol{E}_{Fund}$||**a** (green line)), although the THG shows the usual polarization which is the same as that of the fundamental pulse as shown in the lower panel of Fig. 10(a). Such unusual polarization dependence of the SHG cannot be reproduced by the theory, i.e., I_{SH} (theory) shows the polarization that is parallel to the fundamental polarization for both $\boldsymbol{E}_{fund}$ ||**c** and $\boldsymbol{E}_{fund}$||**a**. The polarization dependence cannot be understood simply by a point group analysis of $\chi^{(2)}$ tensor for the orthorhombic structure (class mm2(C_{2v}) (after due consideration of the symmetry breaking uniaxially induced by the current $\boldsymbol{j}$)). To demonstrate a response of $\boldsymbol{j}$||**c** ($\boldsymbol{E}_{pr}$||**c**) under the excitation polarization of $\boldsymbol{E}_{pu}$||**a**, we investigate the polarization dependence of a transient reflectivity (pump-probe) measurement. As shown in Fig. 10(b), the responses of $\boldsymbol{E}_{pr}$||**c** are larger than $\boldsymbol{E}_{pr}$||**a** for both $\boldsymbol{E}_{pu}$||**a** and $\boldsymbol{E}_{pu}$||**c** ($\boldsymbol{E}_{pu}$ and $\boldsymbol{E}_{pr}$ are the electric fields of pump- and probe- lights, respectively). Therefore, it is clear that light-induced charge motion occurs easily along the c-axis for both $\boldsymbol{E}_{pu}$||**a** and $\boldsymbol{E}_{pu}$||**c**. The similar polarization dependence has also been observed in κ-(BEDT-TTF)$_2$Cu[N(CN)$_2$]Cl (insulating phase) even under a weaker excitation condition of 3.1 eV (probe energy=1.55 eV)[46]. Thus, the results of the transient reflectivity measurements do not contradict the above results of the SHG.

The observation of the SHG induced by the no-scattering current suggests a possibility of even-order HHG. However, absorption losses sometimes prevent the observation of HHG in thick bulk crystals. In fact, intramolecular transitions exist in the spectral region of the HHG in this compound. We attempt to detect a non-linear polarization in the material through interplay between the polarizations of SHG/THG and HHGs (without a direct detection of HHGs). Here, the essence of 2-D spectroscopy is used. As shown in Fig. 11(a), a pair of pulses with a time difference of Δt enters the material and emitted lights including SHG and THG are detected by changing Δt with an accuracy of 100 attoseconds and by utilizing the TWINS technique [28-31] as described above. The obtained light intensity as a function of Δt is referred to as an interferogram. In 2-D spectroscopy [28-31], the Fourier transformed (FT) spectrum of the interferogram is plotted parallel to the ordinate for respective detection energies in the abscissa as schematically shown in Fig. 11(b). In the non-linear 2-D spectrum of Fig. 11(b), off-diagonal components such as (2H, 4H) and (3H, 4H) should show the interplay between 2H and 4H or 3H and 4H, respectively.

Figure 11(c) shows the Fourier spectra of the interferograms (modulation of SHG and THG intensities as a function of Δt) detected at 1.5 eV (SHG, red dots) and 2.25 eV (THG, blue dots). We notice the peak at 3 eV corresponding to (2H, 4H) and (3H, 4H) in Fig. 11(b). The results show that a polarization of the 4-th harmonic is generated in the material and modulates the lower order polarizations (of SHG

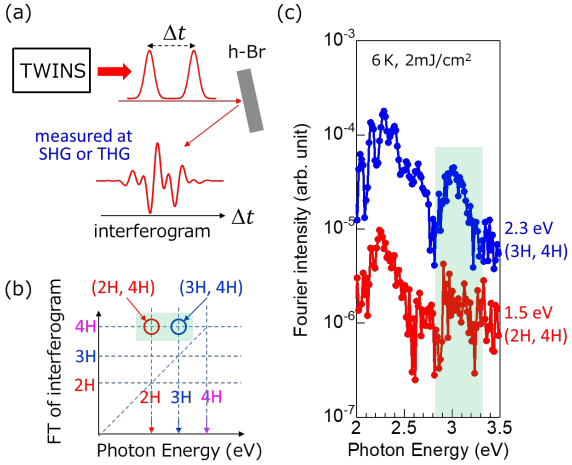

Fig. 11 (a) Schematic illustration of experimental configuration using TWINS. (b) Schematic illustration of 2-D spectroscopy, where 2H, 3H and 4H represent the energies of SHG, THG and 4-th harmonic generation. (c) Fourier spectra of interferograms (modulation of SHG and THG intensities as a function of Δt) detected at 1.5 eV(SHG, red dots) and 2.25 eV(THG, blue dots).

and THG). In general, it is difficult to measure HHG in thick bulk crystals because of absorption losses. The method shown here without a direct measurement of HHGs in thin films is expected to be useful for investigating the non-linear polarizations which potentially induce HHGs.

Finally, we consider the relation between the no-scattering current and superconducting fluctuations. The above-mentioned equation $\boldsymbol{j}(\boldsymbol{t}) \propto \int_0^t \boldsymbol{E}(\tau)\boldsymbol{d}\tau$ is justified only in the ultrafast no-scattering time window. In principle, the no-scattering mechanism of the SHG discussed above is not necessarily limited to the superconducting materials. Indeed, as shown in Fig. 7(a), the SHG increases toward T_{SC}, indicating that the no-scattering current is closely related to superconducting fluctuations. Considering that the time integral of $\boldsymbol{E}$(t) is the vector potential $\boldsymbol{A}$(t) in the present choice of a gauge, we notice the similarity between the above equation and the London equation $\boldsymbol{j}(\tau) = -(\mathbf{n_s}\boldsymbol{e}^2/\mathbf{m})\,\boldsymbol{A}$ (m: mass of superconducting electrons, n_s: number density of superconducting electrons, e: elementary charge) phenomenologically describing the Meissner effect. We cannot easily compare the above two equations for $\boldsymbol{j}$ because the no-scattering current and the London equation are based on the different conditions (former: local and ultrafast time scale, latter: global and in near-equilibrium). However, the similarity between these two equations suggests that the ultrafast charge dynamics during the no-scattering time window is closely linked to superconducting fluctuations.

Conclusions

The stimulated emission and the SHG in an centrosymmetric organic conductor (κ-(h-ET)$_2$Cu[N(CN)$_2$]Br) under the application of a 6-fs strong light field are respectively induced by a synchronized charge oscillation and a no-scattering current. These results indicate that correlated charge motion can be driven in a manner which is very different from the conventional photoinduced charge dynamics with scattering processes. Such no-scattering charge dynamics have been hidden behind the increase in the electron temperature. The fact that the stimulated emission and the SHG show the anomalous enhancements towards T_{SC} indicates that these ultrafast nonlinear phenomena are related to T_{SC} and/or superconducting fluctuations. The < 5 fs rise of the stimulated emission and its temperature dependence indicate that the microscopic mechanism of superconducting fluctuations is related to Coulomb repulsive interactions. Furthermore, we also observe the 4-th order polarization through the interplay between the polarizations of SHG/THG and HHGs, i.e., without directly detecting the 4-th order harmonic generation.

Conflicts of interest

There are no conflicts to declare.

Acknowledgements

The authors thank Professor T. Sasaki (Institute for Materials Research, Tohoku University) and Professor H. M. Yamamoto (Institute for Molecular Science) for providing single crystals and a thin film of κ-(h-ET)$_2$Cu[N(CN)$_2$]Br. The authors also thank Professor H. Kishida (Nagoya University) for measuring and analyzing steady state optical spectra. This work was supported by JST CREST (JPMJCR1901), MEXT Q-LEAP (JPMXS0118067426).

Notes and references

1 M. Imada, A. Fujimori, and Y. Tokura, *Rev. Mod. Phys*. 1998, **70**, 1039.
2 D. N. Basov and T. Timusk, *Rev. Mod. Phys*. 2005, **77**, 721.
3 T. Ishiguro, K. Yamaji, and G. Saito, *Organic Superconductors*, Springer 1998.
4 C. Giannetti et al., *Advances in Physics* 2016, **65**, 58.
5 R. Matsunaga et al., *Science* 2014, **345**, 1145.
6 A. Cavalleri, *Contemporary Physics* 2018, **59**, 31.
7 D. N. Basov, R. D. Averitt & D. Hsieh, *Nat. Matter*. 2017, **16**, 1077.
8 S. Koshihara et al., *Phys. Rep*. 2022, **942**, 1.
9 Y. Kawakami et al., *Phys. Rev. Lett*. 2010, **105**, 246402.
10 T. Ishikawa et al., *Nat. Commun*. 2014, **5**, 5528.
11 Y. Naitoh et al., *Phys. Rev*. 2016, **B93**, 165126.
12 Y. Kawakami et al., *Phys. Rev*. 2017, **B95**, 201105(R).
13 Y. Kawakami, et al., *Nat. Photon*. 2018, **12**, 474.
14 Y. Kawakami, et al., *Nat. Commun*. 2020, **11**, 4138.
15 K. Kanoda, *Hyperfine Interactions* 1997, **104**, 235.
16 T. Mori, H. Mori, & S. Tanaka, *Bull. Chem. Soc. Jpn*. 1999, **72**, 179.
17 M. Watanabe et al. *Synth. Met*. 1999, **103**, 1909.
18 F. Kagawa, K. Miyagawa, and K. Kanoda, *Nature* 2005, **436**, 534.
19 B. J. Powell and R. H. McKenzie, *J. Phys. Condens. Matter* 2006, **18**, R827.
20 T. Sasaki et al., *Phys. Rev*. 2004, **B69**, 064508.
21 D. Faltermeier et al., *Phys. Rev*. 2007, **B76**, 165113.
22 M. Lang, F. Steglich, N. Toyota, & T. Sasaki, *Phys. Rev*. 1994, ***B*49**, 15227.
23 T. Kobayashi, Y. Ihara, Y. Saito, A. Kawamoto, *Phys. Rev.* 2014*,* ***B*89**, 165141.
24 H. M. Yamamoto et al., *Nat.* Commun. 2013, **4**, 2379.
25 H. Telle et al., *Appl. Phys*. 1999, **B69**, 327.
26 F. W. Helbing et al., *Appl. Phys*. 2002, **B74**, s35.
27 M. Mehendale et al., *Opt. Lett*. 2000, **25**, 1672.
28 D. Brida, C. Manzoni, and G. Cerullo, *Opt. Lett*. 2012, **37**, 3027.
29 J. Rehault et al., *Rev. Sci. Ints*. 2014, **85**, 123107.
30 A. De Sio et al., *Nat. Commun*. 2016, **7**, 13742.
31 J. M. Richter et al., *Nat. Commun*. 2017, **8**, 376
32 M. Dressel, N. Drichiko, *Chem. Rev*. 2004, **104**, 5689.
33 J. E. Eldridge et al. *Spectrochimica Acta* 1996, **A52**, 45.
34 Y. Matsubara et al. *Phys. Rev.* 2014, ***B*89**, 161102(R).
35 H. Sasaki et al. *Sci. Rep*. 2018, **8**:9609.
36 K. Yonemitsu, *J. Phys. Soc. Jpn*. 2018, **87**, 044708.
37 K. Yonemitsu, *J. Phys. Soc. Jpn*. 2018, **87**, 124703.
38 T. Shimada, and K. Yonemitsu, *J. Phys. Soc. Jpn*. 2020, **89**, 084701.
39 K. Yonemitsu, and P. Werner, *J. Phys. Soc. Jpn.*, 2021, **90**, 044713.
40 Y. Nakazawa, et al., *Phys. Rev*. 2000, **B61**, 16295.
41 A. Y. Bykov et al., *Phys. Rev*. 2012, **B85**, 121413(R).
42 M. Tokman et al., *Phys. Rev*. 2019, **B99**, 155411.
43 C. Vaswani et al., *Phys. Rev. Lett*. 2020, **124**, 207003.
44 R. E. F. Silva, et al. *Nat. Photon*. 2018, **12**, 266-270.

45 Y. Murakami, M. Eckstein, & P. Werner, *Phys. Rev. Lett*. 2018, **121**, 057405.
46 S. Tsuchiya et al., 2019, *J. Phys. Soc. Jpn*. **88**, 074706.